NANO LETTERS

Letter

pubs.acs.org/NanoLett

Plasmonic Waveguide Ring Resonators with 4 nm Air Gap and λ_0^2/15 000 Mode-Area Fabricated Using Photolithography

Jaehak Lee,[†] Juhee Song,[§] Gun Yong Sung,[∥] and Jung H. Shin*[,†,‡]

[†]Department of Physics and [‡]Graduate School of Nanoscience and Technology, KAIST 373-1 Guseong-dong, Yuseong-Gu, Daejeon, South Korea

[§]Biosensor Research Team, ETRI, Daejeon 305-700, South Korea

[∥]Department of Materials Science and Engineering, College of Information and Electronic Engineering, Hallym University, 1 Hallymdaehak-gil, Chuncheon, Gangwon-do 200-702 Republic of Korea

Supporting Information

ABSTRACT: Plasmonic air-gap disk resonators with 3.5 μm diameter and a 4 nm thick, 40 nm wide air gap for a mode area of only λ_0^2/15 000 were fabricated using photolithography only. The resonant modes were clearly identified using tapered fiber coupling method at the resonant wavelengths of 1280−1620 nm. We also demonstrate the advantage of the air-gap structure by using the resonators as label-free biosensors with a sensitivity of 1.6 THz/nm.

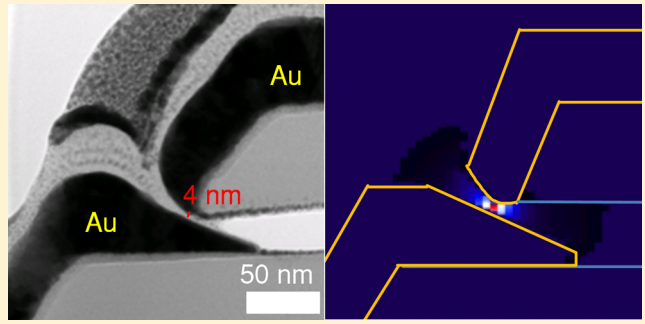

KEYWORDS: *Plasmonics, microcavity, nanofabrication, biosensor*

Subwavelength confinement of light has been the subject of intense research.[3−7] By providing a highly enhanced E-field in a very small volume, it can allow control over and investigation into fundamental optical properties such as radiative transition rates as well as enable many diverse applications such as highly efficient lasers,[8−10] sensors,[11−13] and optical traps.[14] Of the many possible methods of confining light[1,2,8,15,16] metal−insulator−metal (MIM) structure has attracted much attention as it can provide both the strong, plasmonic light confinement for a small mode volume and a reasonably long propagation distance.[17,18] By now, many devices such as sensors,[19] lasers,[20] optical circuits,[21,22] and optical traps[23,24] that take advantage of such an MIM structure have been reported. In most cases, a vertical MIM structure is used in which a thin gap is etched through a metal film using either focused ion-beam (FIB) or electron-beam lithography. They offer the advantages of precise drawing of the gap but are highly demanding in both cost and time and also are difficult to scale up to a large-scale fabrication. Thus, there have been attempts at defining a horizontal MIM structure in which an insulating spacer layer is stacked between two metal layers via sequential deposition. In this case, the insulating layer can be extremely thin as it is defined simply by deposition time. Furthermore, as the metal−insulator interface is defined by deposition, it can be much smoother than that defined by lithography and etching. Using such horizontal MIM structure, ultrasmall mode volume microcavities have been demonstrated.[20,25−27]

However, the need for an insulating layer can significantly limit the application of such horizontal MIM structures, as the region of highest light intensity is locked inside the deposited spacer material and is unavailable for further access from outside. Furthermore, lateral confinement still requires the same high resolution lithography that the horizontal structure seeks to avoid. Without such additional steps, the plasmon modes extend across the entire structure, leading to large overall mode sizes and multiple higher order modes.[25] In this paper, we report on fabrication and application of MIM disk resonators with empty air gaps in which the E-fields of the modes are mostly confined along the circumference of the disk. Arrays of disk resonators with a narrow MIM air-gap ranging from 40 to 4 nm could be fabricated on a large scale using only simple photolithography, selective etching, and directional deposition. The plasmonic resonant modes whose E-field was concentrated in the nanometer-thin slot along the circumference of the disk were clearly identified using tapered fiber coupling method[1,2] with measured Q-factors of 10−20 at the resonant wavelengths of 1280−1620 nm. The cross-sectional mode area was calculated to be λ_0^2/15 000 with the possibility of further reduction to ~λ_0 /40 000. Finally, we demonstrate the advantage of the air-gap structure by using the resonators as label-free biosensors with a sensitivity of 1.6 THz/nm.

Received: May 21, 2014
Revised: August 30, 2014

   dx.doi.org/10.1021/nl5018892 | *Nano Lett.* XXXX, XXX, XXX−XXX

To fabricate the air-slot resonators, a silicon nitride (SiN_x)/silicon oxide (SiO_2)/silicon nitride (SiN_x) multilayer was first deposited on an oxidized Si wafer using reactive ion-beam sputtering method.[1] The SiN_x layer thickness was kept constant at 65 nm but the SiO_2 layer thickness was varied to be between 40 and 70 nm. The thickness of the thermal oxide of the substrate was 5.0 μm. After the multilayer deposition, circular disk patterns with a nominal diameter of 3.5 μm were made using photolithography with MA6 contact aligner and 365 nm light. Subsequent reactive ion etching at 12 mTorr pressure with CHF_3 and SF_6 gas was used to fabricate the dielectric disks. The total etch depth was set to 800 nm to completely etch through the multilayer film and expose the underlying oxide substrate. Finally, an isotropic etching using buffered hydrofluoric acid was used to selectively etch into the SiO_2 spacer layer as well as the oxide substrate, defining an air-slot between the edges of the SiN disks as well as the central support post. It is important to note here that due to the effect of diffraction the sidewalls of the photoresist pattern, and subsequently the etched disk patterns, are sloped inward. Thus, the top disk is slightly smaller in diameter than the bottom disk and, upon formation of the air-slot, exposes the edge of the bottom disk when viewed from the top. Consequently, when the final Cr adhesion and Au layers are deposited using DC sputter at a pressure of 1 mTorr to thicknesses of 5 and 30−85 nm, respectively, the top disk acts as a shadow mask except for a narrow ring along the circumference of the bottom disk. The final structure is thus a narrow metal ring aligned with and suspended below an inverted pie-pan shaped metal disk, separated by an air-gap. The fabrication procedure, together with a schematic of the fabricated structure, is summarized in Figure 1.

Figure 2a shows a scanning electron microscope (SEM) image of a typical resonator. Isolation of the disk by the central SiO_2 post and formation of air-gap can be seen. To observe the cross-section of the MIM structure, FIB milling was done across center of the disk. Figure 2b shows the cross-section transmission electron microscope (TEM) image of the same resonator, showing the air gap in detail. We note that the apparent filling of the gap and presence of additional dark metal layers surrounding the gap are due to the required deposition of protective material prior to FIB milling and not related to the actual resonator structure. Also shown in Figure 2c is the energy-dispersive X-ray spectroscopy image of the same air-gap, clearly delineating the coverage of the resonator by deposited gold. Several points are worthy of note. First, despite the shadowing by the top disk, the bottom gold ring extends slightly into the gap below the top SiN disk. Second, due to the self-shadowing effect[28] the bottom edge of the top gold disk forms a rounded tip opposite the top surface of the bottom ring. Finally, as the air-gap is defined by deposition, gold surfaces are quite smooth. As shown in Figure 2d that shows the atomic force microscope (AFM) image of a typical gold deposited surface, the root-mean-square (RMS) roughness is 0.8 nm only. As a result, a T-shaped MIM structure with a thin air-gap can be defined between the bottom edge of the top disk and the bottom ring. Indeed, as Figure 2c,e shows, the thickness of the air-gap, defined to be the shortest distance between the two metal parts of the MIM resonator, can be controlled from 40 to 20 nm, 13 nm, and all the way down to 4 nm simply by controlling the thickness of the sacrificial SiO_2 spacer layer.

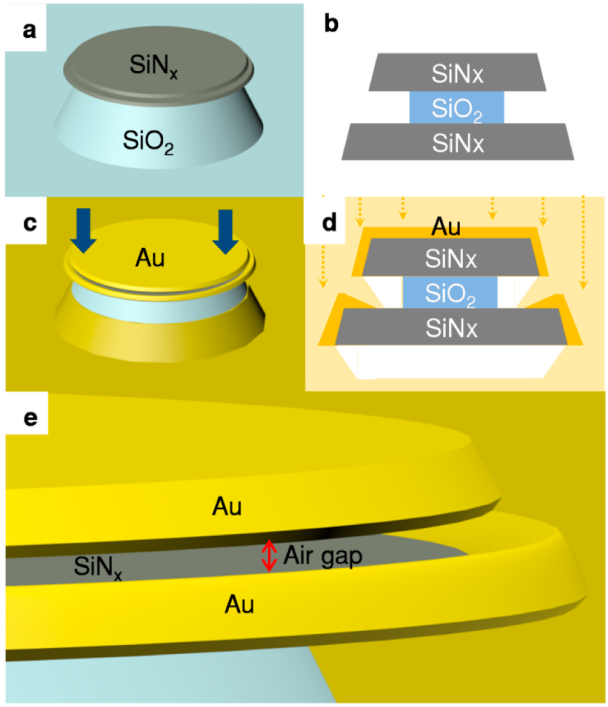

Figure 1. Schematic of the plasmonic ring resonator. (a) Schematic of a pedestal-type SiN_x slot disk resonator with air-slot and silica post. (b) The cross-sectional view is shown. (c) Schematic of the plasmonic ring resonator after directional DC sputtering of Au. Arrows indicate the direction of the deposition. (d) The cross-sectional view, indicating the effect of self-shadowing. (e) Detailed schematic view on the MIM gap of the plasmonic ring resonator. The red arrow indicates the air-gap formed between the bottom edge of the top disk and top surface of bottom ring.

On the basis of the measured disk structure, the optical modes are calculated using the finite-difference time-domain (FDTD) method. Figure 3a,b shows that the mode is indeed concentrated in the air-gap. More importantly, the thinness of the down-turned sidewalls of the top gold metal disk, together with its rounded tip, strongly concentrates the mode at the bottom edge of top disk, resulting in a strong lateral confinement as well, for a mode width as narrow as 40 nm. As a result, the cross-sectional mode area is extremely small: the mode area of the 40 nm gap resonator is calculated to be 1700 nm^2, corresponding to mode area of $\lambda_0^2/1\,200$, where λ_0 is the vacuum wavelength, while that of the 4 nm gap resonator is 130 nm^2, or $\lambda_0^2/15\,000$. These are among the lowest values reported for air-gap plasmon resonators. For instance, a comparable MIM structure with two horizontal metal disks[25] is calculated to have a mode area of $\lambda_0^2/3\,000$ as well as many higher order modes, and a cylindrical metal nanowire on top of a metal film[20] would have a mode area of $\lambda_0^2/12\,500$. Such concentration of mode in the air-gap also indicates that the mode is an antisymmetric mode, where the charges on the opposite side modes in which the charges of the two metal surfaces facing each other have opposite signs. This is confirmed by Figure 3c, which shows that the maximum electric field, as determined by the FDTD simulations, points directly across the air-gap.

In general, a MIM disk resonator structure may support many other modes such as a symmetric mode in which the charges of the two metal surfaces facing each other have the same sign,[29] higher order radial modes,[25] and hybrid modes.[2]

dx.doi.org/10.1021/nl5018892 | Nano Lett. XXXX, XXX, XXX−XXX

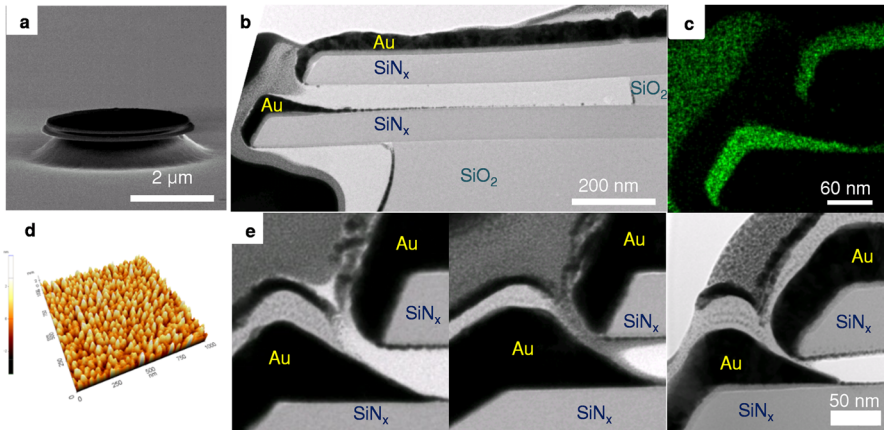

Figure 2. Microscope images of the plasmonic ring resonator. (a) SEM image of the same sample with ~10° tilt from the substrate. (b) TEM crosssection image of the same sample obtained after FIB milling that was done across center of the disk. Black region on the disk indicates the deposited Au. Gray and black material surrounding the disk are protective material deposited prior to FIB milling and not related to the actual resonator structure. (c) An energy-dispersive x-ray spectroscopy mapping image of the same sample. The bright green area indicates the signals of Au. (d) Atomic force microscope (AFM) image of a typical Au film deposited on the SiNx surface. White region indicates >+2 nm from average, and black region indicates <−2 nm from average. The root-mean-square of the height was 0.786 nm. (e) TEM cross-section images of fabricated resonators. From the left, the gap thickness is 20, 13, and 4 nm.

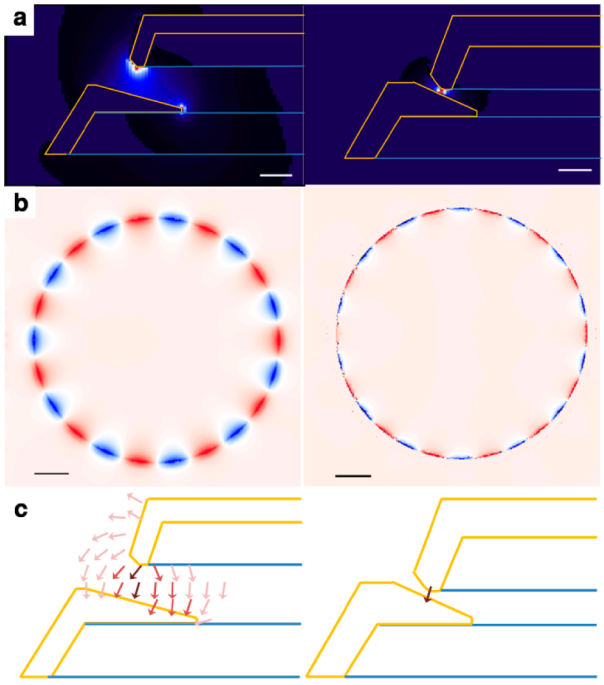

Figure 3. Mode profiles. FDTD calculated mode profiles of the microdisk with 40 nm gap (left) and 4 nm gap (right) at resonance frequencies of 210 THz and 213 THz, respectively. (a) The cross-sectional view of the $|E|^2$ distribution (scale bar =50 nm), while (b) shows the top view of the E_z (TM-component electric field) distribution of same modes at the plane of the air-gap (scale bar = 500 nm). (c) Electric field directions in the cross-sectional view. In sequence of decreasing darkness, the colors of arrows indicate 100, 75, 50, and 25% of maximum E-field intensity.

However, extensive simulations have shown that the anti-symmetric, first-order radial modes characterized by the azimuthal number are the only modes supported by the resonator structure up to ~235 THz (corresponding to vacuum wavelengths of 1.28 μm). The lack of symmetric mode is ascribed to the fact that the resonator structure itself is highly asymmetric; the top metal structure is essentially a disk with a continuous metallic connection across the top of the SiN_x disk to the opposite sides, while the bottom metal structure is a ring of finite width. The lack of higher order radial modes is ascribed to the small radius of the resonator and the narrow width of the bottom ring relative to the wavelength. In fact, the resonator begins to support higher order radial modes at frequencies in excess of 250 THz or at wavelengths shorter than 1.2 μm. More detailed discussion of the simulations results regarding the optical modes can be found in Supporting Information S1.

The presence of the calculated plasmon modes were confirmed directly using a U-bent tapered fiber with a nominal diameter of 1 μm.[1,11] Unpolarized light from a supercontinuum light source (VIS-NIR) was used as the light source, and the transmitted intensity was collected using optical spectral analyzer on the NIR range (185−235 THz). In all cases, the coupling fiber was in a contact with the microdisk, typically next and below the disk in order to match the E-field direction. A schematic description of the coupling setup is shown in Figure 4a, and a more detailed discussion about fiber coupling method can be found in Supporting Information S2. Figure 4b,c shows the results for the resonators with 40 and 4 nm thin air gaps, respectively. In all cases, the intensities are normalized to uncoupled intensity. Also shown are the calculated resonances obtained from the FDTD simulations. We find a series of periodic dips, indicating excitation of resonances. The shape of the transmission spectra is very simple, indicating only a single set of resonant modes, which is in agreement with calculated results. The positions of the dips also agree very well with the positions of the WGM resonances calculated by FDTD simulations, again indicating that the observed dips are due to excitation of the antisymmetric WGMS mode shown in Figure 3.

To further confirm that the observed dips are indeed the WGM resonances and to demonstrate the advantage of the air-gap MIM ring structure, we demonstrate the operation of the air-gap MIM ring resonator as a biosensor using an IgG type antibody (monoclonal prostate-specific antigen (PSA) antibody) and bovine serum albumin (BSA) as adsorbed protein specimens. Two resonator samples were prepared. One 40 nm gap resonator was put in a PSA antibody solution with a

dx.doi.org/10.1021/nl5018892 | Nano Lett. XXXX, XXX, XXX−XXX

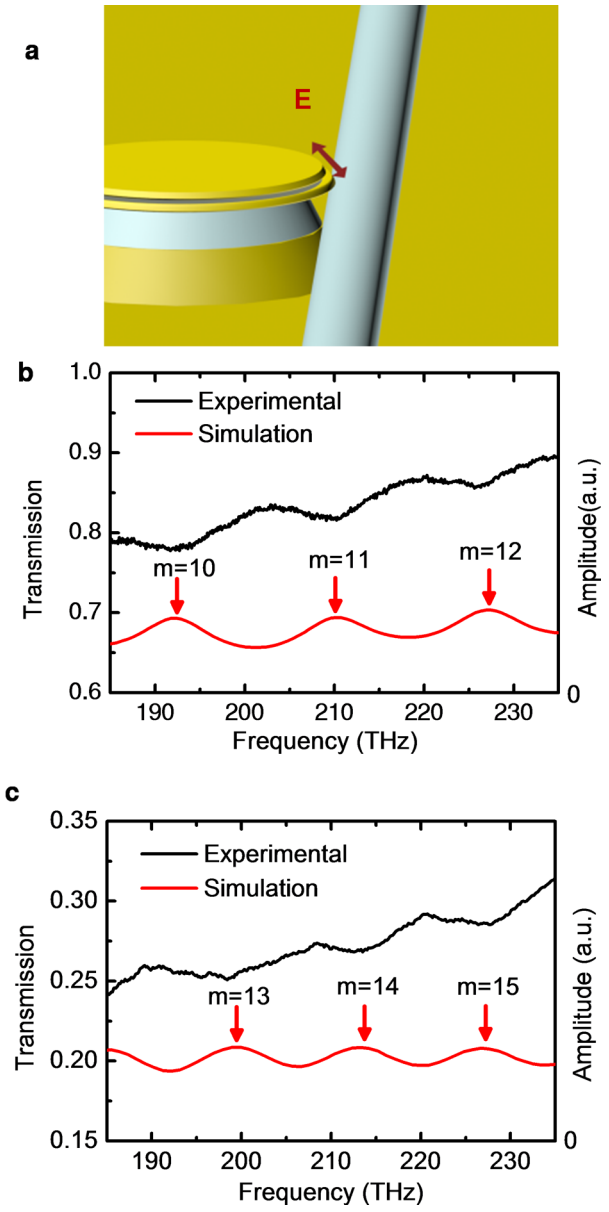

Figure 4. Transmission spectra of the plasmonic ring resonators. (a) Schematic of tapered fiber coupling measurement. Red arrow indicates the electric field direction of the plasmonic mode. (b,c) Spectral responses of microdisks with (b) 40 nm gap and (c) 4 nm gap from experiment and simulation. Black solid lines are the transmission spectra obtained by tapered fiber coupling. The intensity is normalized to the uncoupled values. Note the periodic dips, indicative of excitation of resonance modes. Red solid lines are resonance spectra obtained by Fourier transform of the electric field at FDTD simulation on same structures. Red arrows indicate the resonance frequencies of the whispering gallery modes with their azimuthal symmetry numbers as obtained from a FDTD simulation.

concentration 100 μg/mL for 24 h and then rinsed with DI water. Subsequently, it was blow dried with nitrogen, and its plasmon resonances measured. The other resonator underwent an additional treatment in a 10% BSA solution for an hour before being rinsed with DI water, dried, and its plasmon resonances measured. Both the PSA antibodies and BSA molecules bond chemically with gold via the amine ($-NH_2$) functional group of lysine residues, leading to formation of a self-assembled monolayer[30,31] on the gold surface, which in turn changes the effective index of the resonance modes and subsequent shifts in the resonance positions. Assuming a refractive index of 1.45, we calculate a surface sensitivity of 1.6 THz/nm, which is more than double that reported for a comparable dielectric resonator.[11]

Figure 5a,b shows the effect of the PSA antibody and BSA layer formation on the transmission, spectra, respectively. The

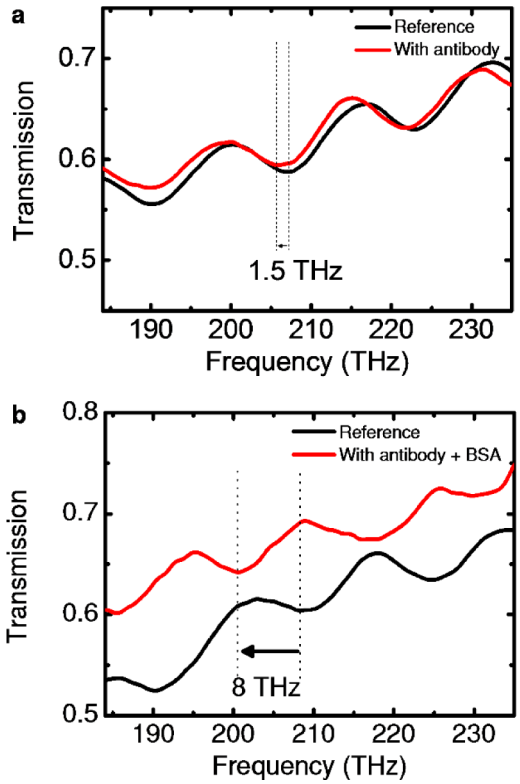

Figure 5. Biosensing experiment. (a) Transmission spectra of a 40 nm gap disk before (black) and after (red) being stayed in a 100 μg/mL PSA antibody solution for 24 h. A clear redshift of 1.5 THz is observed. (b) Transmission spectra of a 40 nm gap disk before (black) and after (red) being stayed in a 10% BSA solution for an hour. A clear redshift of 8 THz is observed. The transmission spectra were smoothed using Sevitzky−Golay method to determine the dip center more clearly, and all spectra were obtained in air after drying the disks.

transmission spectra were smoothed using Sevitzky−Golay method to determine the dip center more clearly (raw data are provided in Supporting Information S3. In all cases, the resonance dips shift uniformly. For PSA antibody, we observe a small shift of 1.6 THz, corresponding to a nominal layer thickness of 0.9 nm, while for BSA, a much larger shift of 8 THz, corresponding to a nominal layer thickness of 5 nm, is observed. Such a uniform shift of the resonance dips upon modification of the environments is another strong indication that they are indeed the plasmonic air-gap modes and that they can be used for many diverse applications where access to highly confined optical modes are desired. The reason for the smaller shift of PSA antibody relative to the BSA layer is not clear, as the solution concentrations in both cases were sufficient to result in near saturation. It may be due to the slightly larger size of the PSA antibody over BSA, or because in the case of the PSA antibody the lysine residues responsible for attaching to gold surfaces are found only at the ends, while in the case of BSA they are distributed all over the surface. Still,

dx.doi.org/10.1021/nl5018892 | Nano Lett. XXXX, XXX, XXX−XXX

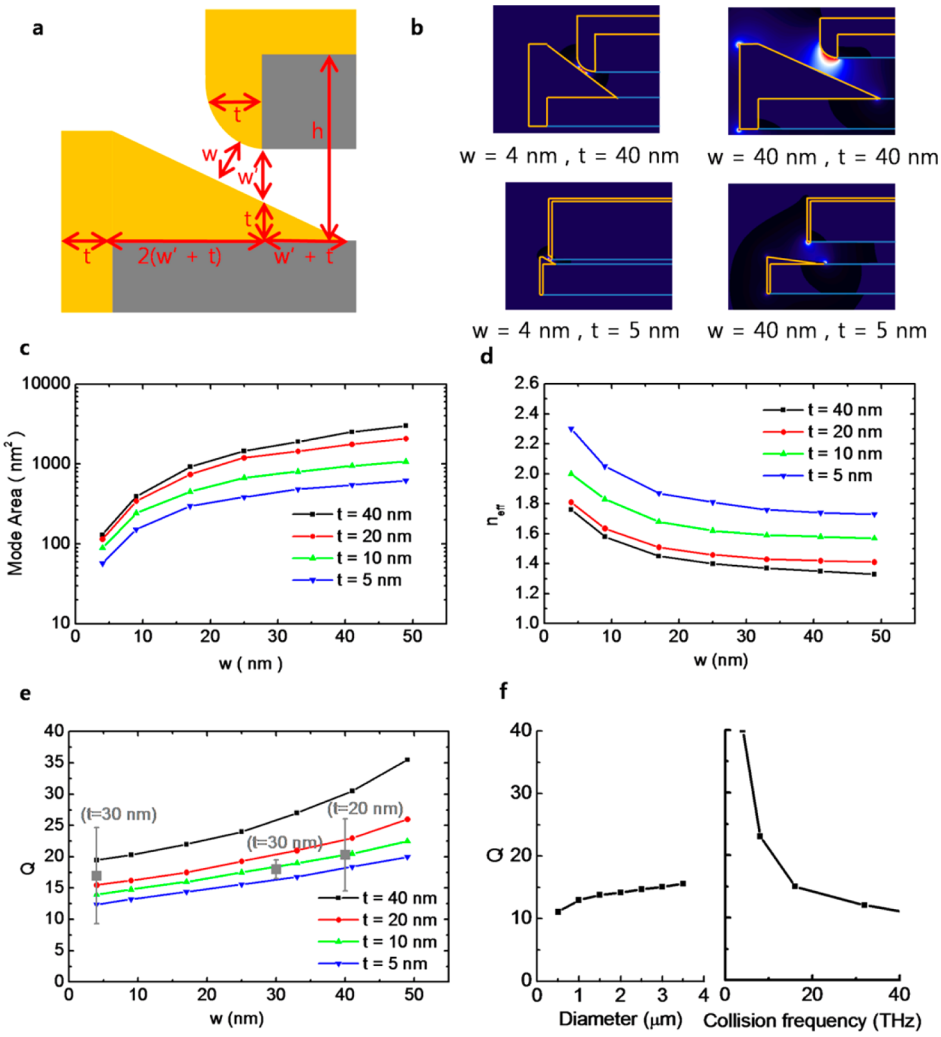

Figure 6. Mode properties for structures. (a) Conceptual figure of the cross-sectional view of the MIM resonators with the structural parameters *w*, *t* and *h*. In all calculations in Figure 6, *h* is fixed as 130 nm. (b) Calculated cross-sectional mode profiles of the MIM resonators with various structure parameters. (c) Calculated mode areas. (d) Effective indices. (e) Simulated (solid lines with symbols) and measured (symbols with error bars and metal tip widths) *Q*-factors of the MIM resonators with various metal thickness and slot width are shown. (f) *Q*-factors of the MIM resonator with *w* = 4 nm and *t* = 20 nm at various diameters and collision frequencies.

such differences also indicate that careful optimization of the air-gap structure and functionalization steps would be necessary for each application. A more detailed discussion on the biosensing experiments can be found in Supporting Information S3.

Figure 6 shows the results of one such structural optimization, where we investigated the dependence of the mode properties on the air-gap thickness "*w*" and the metal tip width "*t*". The structural variables are summarized in Figure 6a. In all calculations, we assumed the shape of upper metal tip to be a quarter circle with radius *t*. On the basis of the TEM images of the real samples, we also assumed the difference in radius between the upper and lower SiN_x disks to be twice the spacer layer thickness ($w' + t$). Figure 6b–e shows the result of varying air-gap width and metal tip width while keeping the overall resonator height "*h*" and disk radius fixed at 130 nm and 1.75 μm, respectively. We find that decreasing the air-gap width and/or the metal tip width strongly decreases the mode area from 3100 nm^2 for a resonator with an air-gap width and metal tip width of 50 and 40 nm, respectively, to 57 nm^2 for a resonator with an air-gap width and metal tip width of 4 and 5 nm, respectively. On the other hand, the effect varying the resonator structure on the effective mode index and the cavity *Q*-factor is rather small, as the same change in the air-gap width and metal thickness increases the mode index from 1.33 to 2.6 and decreases the *Q*-factor from 36 to 12 only. Experimentally observed *Q*-factors also fall within this range, although the agreement with the theoretically predicted values is not exact. This indicates that the cavity *Q*-factor is dominated by the metal loss. Indeed, as Figure 6f shows, the cavity *Q*-factor changes from 16 to 11 only as the disk radius is decreased from 3.5 to 0.5 μm but increases strongly from 12 to 40 as the collision frequency (e.g., metal loss) is reduced from 32 to 4 THz. Thus, the results indicate that for applications where a high *Q*-factor is desired, priority should be given to reduce the metal loss (e.g., by reducing the surface roughness and/or using a metal with lower collision frequency such as silver).

In conclusion, we have designed and fabricated 3.5 μm diameter MIM ring resonators with T-shaped air-gap along its circumference using simple photolithography and selective etching only. Self-aligned formation of 10 nm scale features were induced by self-shadowing effect, and confinement of

dx.doi.org/10.1021/nl5018892 | *Nano Lett.* XXXX, XXX, XXX−XXX

optical mode into a mode area as small as $\lambda_0^2/15\,000$ achieved with possibility of further reduction to $\lambda_0/40\,000$. The measured resonance dips were also verified by demonstrating application of the resonator structure for biosensing experiment. Such confinement of electric field on air-region with ultrasmall mode area may be used in many other applications such as nonlinear optics, optical trapping, and biosensing.

■ ASSOCIATED CONTENT

Supporting Information

Additional FDTD and FEM simulations for symmetric modes and radial higher order modes of the MIM resonators, calculations on other possible horizontal MIM structures, details about tapered fiber coupling methods, detailed information about PSA antibody and BSA, simulation result on surface sensitivity, and the unsmoothed raw data of Figure 6. Also supporting figures are provided (Figures S1−S9). This material is available free of charge via the Internet at http://pubs.acs.org.

■ AUTHOR INFORMATION

Corresponding Author

*E-mail: jhs@kaist.ac.kr. Tel.: +82-42-350-5538. Fax: +82-42-350-2510.

Author Contributions

J.L. designed and performed experiments, analyzed data, and wrote the paper. J.S. performed bioexperiments. G.Y.S. analyzed the data. J.H.S. designed experiments, analyzed data, and wrote the paper. All authors have given approval to the final version of the manuscript.

Funding

This work was supported in part by the National Research Foundation of Korea (NRF) grant funded by the Korea government (MSIP) (Grant 2010−0029255).

Notes

The authors declare no competing financial interest.

■ REFERENCES

(1) Lee, S.; Eom, S. C.; Chang, J. S.; Huh, C.; Sung, G. Y.; Shin, J. H. *Opt. Express* **2010**, *18*, 11209−11215.
(2) Min, B.; Ostby, E.; Sorger, V.; Ulin-Avila, E.; Yang, L.; Zhang, X.; Vahala, K. *Nature* **2009**, *457*, 455−458.
(3) Barnes, W. L.; Dereux, A.; Ebbesen, T. W. *Nature* **2003**, *424*, 824−830.
(4) Lal, S.; Link, S.; Halas, N. J. *Nat. Photonics* **2007**, *1*, 641−648.
(5) Yan, R.; Gargas, D.; Yang, P. *Nat. Photonics* **2009**, *3*, 569−576.
(6) Gramotnev, D. K.; Bozhevolnyi, S. I. *Nat. Photonics* **2010**, *4*, 83−91.
(7) Atwater, H. A.; Polman, A. *Nat. Mater.* **2010**, *9*, 205−213.
(8) Oulton, R. F.; Sorger, V. J.; Zentgraf, T.; Ma, R. M.; Gladden, C.; Dai, L.; Bartal, G.; Zhang, X. *Nature* **2009**, *461*, 629−632.
(9) Noda, S.; Fujita, M.; Asano, T. *Nat. Photonics* **2007**, *1*, 449−458.
(10) Berini, P.; De Leon, I. *Nat. Photonics* **2011**, *6*, 16−24.
(11) Lee, S.; Eom, S. C.; Chang, J. S.; Huh, C.; Sung, G. Y.; Shin, J. H. *Opt. Express* **2010**, *18*, 20638−20644.
(12) Roh, S.; Chung, T.; Lee, B. *Sensors* **2011**, *11*, 1565−1588.
(13) Feng, J.; Siu, V. S.; Roelke, A.; Mehta, V.; Rhieu, S. Y.; Palmore, G. T.; Pacifici, D. *Nano Lett.* **2012**, *12*, 602−609.
(14) Juan, M. L.; Righini, M.; Quidant, R. *Nat. Photonics* **2011**, *5*, 349−356.
(15) Vahala, K. J. *Nature* **2003**, *424*, 839−846.
(16) Verhagen, E.; Polman, A.; Kuipers, L. K. *Opt. Express* **2008**, *16*, 45−57.
(17) Zia, R.; Selker, M. D.; Catrysse, P. B.; Brongersma, M. L. *J. Opt. Soc. Am. A* **2004**, *21*, 2442−2446.
(18) Veronis, G.; Fan, S. *Opt. Lett.* **2005**, *30*, 3359−3361.
(19) Lee, K. L.; Lee, C. W.; Wang, W. S.; Wei, P. K. *J. Biomed. Opt.* **2007**, *12*, 044023.
(20) Russell, K. J.; Liu, T.-L.; Cui, S.; Hu, E. L. *Nat. Photonics* **2012**, *6*, 459−462.
(21) Fu, Y.; Hu, X.; Lu, C.; Yue, S.; Yang, H.; Gong, Q. *Nano Lett.* **2012**, *12*, 5784−5790.
(22) Huang, K. C. Y.; Seo, M.-K.; Sarmiento, T.; Huo, Y.; Harris, J. S.; Brongersma, M. L. *Nat. Photonics* **2014**, *8*, 244−249.
(23) Zhang, W.; Huang, L.; Santschi, C.; Martin, O. J. *Nano Lett.* **2010**, *10*, 1006−11.
(24) Saleh, A. A.; Dionne, J. A. *Nano Lett.* **2012**, *12*, 5581−6.
(25) Kuttge, M.; Garcia de Abajo, F. J.; Polman, A. *Nano Lett.* **2010**, *10*, 1537−1541.
(26) Chang, Y.-C.; Shih-Ming, Wang; Chung, H.-C.; Tseng, C.-B.; Chang, S.-H. *ACS Nano* **2012**, *6*, 3390−3396.
(27) Miyazaki, H.; Kurokawa, Y. *Phys. Rev. Lett.* **2006**, *96*, 097401.
(28) Mohamed, K.; Alkaisi, M. M. *Nanotechnology* **2013**, *24*, 015302.
(29) Veronis, G.; Fan, S. *J. Lightwave Technol.* **2007**, *25*, 2511−2521.
(30) Jiang, D.; Tang, J.; Liu, B.; Yang, P.; Shen, X.; Kong, J. *Biosens. Bioelectron.* **2003**, *18*, 1183−1191.
(31) Brewer, S. H.; Glomm, W. R.; Johnson, M. C.; Knag, M. K.; Franzen, S. *Langmuir* **2005**, *21*, 9303−9307.